

Upper Ocean Sensitivity to Wind Forcing in the South China Sea

E. JOSEPH METZGER*

Naval Research Laboratory, Stennis Space Center, MS 39529-5004, U.S.A.

(Received 8 October 2002; in revised form 24 March 2003; accepted 25 March 2003)

The Naval Research Laboratory (NRL) Layered Ocean Model (NLOM) has been used to investigate the sensitivity of the upper South China Sea (SCS) circulation to various atmospheric wind forcing products. A 1/16° 6-layer, thermodynamic Pacific Ocean north of 20°S version of NLOM has been integrated using observed climatological monthly mean winds (Hellerman and Rosenstein, 1983) and climatologies based on two atmospheric prediction models: the European Centre for Medium-Range Weather Forecasts (ECMWF) and the National Centers for Environmental Prediction (NCEP). ECMWF products include the 10 meter winds (at both 1.125° and 2.5° resolution) and surface stresses (1.125°). The NCEP forcing (1.875°) is a surface stress product. Significant differences exist in the wind stress curl patterns and this is reflected in the upper ocean model response, which is compared to observational data. The model experiments suggest the generation of the West Luzon Eddy is controlled by positive wind stress curl. The degree of Kuroshio intrusion into the SCS, however, is not affected by wind stress curl but is governed by the coastline geometry of the island chain within Luzon Strait. The summertime offshore flow from the Vietnamese coast is present in all simulations but the dipole structure on either side of the jet is variable, even among experiments with similar wind stress curl patterns. The ECMWF surface stresses exhibit spurious coastal wind stress curl patterns, especially in locations with significant orographic features. This manifests itself in unrealistic small scale coastal gyres in NLOM. High resolution basin-scale and coastal models might be adversely affected by these stresses.

Keywords:

- South China Sea,
- numerical modeling,
- sensitivity to wind forcing,
- upper ocean circulation.

1. Introduction

The South China Sea (SCS) is situated off the southeast corner of the Asian continent (Fig. 1) within a monsoon regime. Its upper ocean circulation is dominated by the seasonally reversing winds that typically blow strongly from the northeast during boreal winter and from the southwest during boreal summer. The equinoctial seasons are transitions between these two distinct flow patterns and are characterized by relatively weak, non-unidirectional winds. Several investigators (Wu *et al.*, 1998; Shaw *et al.*, 1999; Liu *et al.*, 2001) indicate wind stress curl as the main driving force of the basin-wide SCS circulation, except near Luzon Strait. Liu *et al.* (2001) describes the upper layer as forced predominantly by wind stress curl on baroclinic planetary waves. They state that the upper ocean flow is in near-instantaneous Sverdrup

balance because of the rapid transit of these baroclinic planetary waves across the basin.

Given the dynamical importance of the wind stress curl, it is imperative that researchers utilizing numerical models of the SCS have accurate wind forcing data. Modelers have a choice of observation-based wind climatologies such as Hellerman and Rosenstein (1983, hereafter HR), the University of Wisconsin-Milwaukee/Comprehensive Ocean-Atmosphere Data Set (da Silva *et al.*, 1994) or the Southampton Oceanography Centre Ocean-Atmosphere climatology (Josey *et al.*, 1998). In addition, wind climatologies and interannual time series can be obtained from numerical weather prediction models such as the National Centers for Environmental Prediction (NCEP), the European Centre for Medium-Range Weather Forecasts (ECMWF) or the Fleet Numerical Meteorology and Oceanography Center. Both types of data sets are subject to their own unique errors/biases and some obvious questions arise. How consistent or different are these wind products? Do the differences between

* E-mail address: metzger@nrlssc.navy.mil

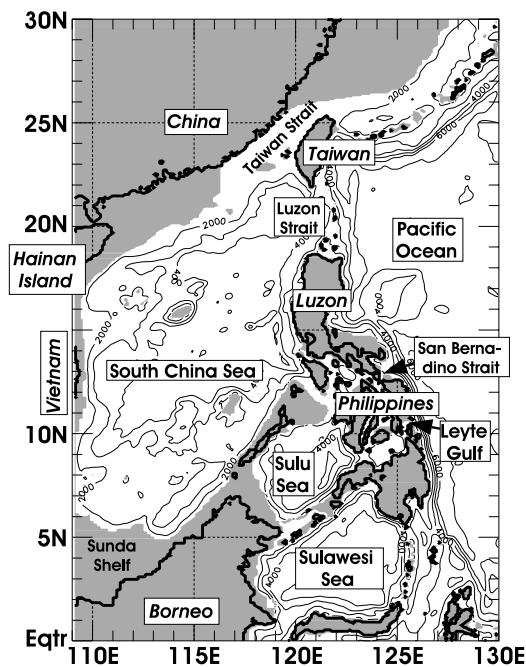


Fig. 1. Model geometry of the South China Sea (SCS) as depicted by NLOM. The gray area is model land and the 200 m isobath generally defines the land/sea boundary, with a few exceptions mentioned in the text. Contours are depths (m) with a 1000 m contour interval.

them affect the upper ocean circulation in the SCS? How sensitive is the ocean model response? It is not the intent of this paper to examine all of these data sets, but to a select few in as consistent a manner as possible, while addressing the questions listed above in the process. Neither is it the intent to declare one product the “winner”, but to point out deficiencies in the wind products that may lead to spurious, model-generated responses. The aim is to provide SCS modelers with a better understanding of how a given atmospheric forcing data set is affecting the underlying simulated ocean, similar to what was done for the Japan/East Sea by Hogan and Hurlburt (2003).

This work builds upon previous SCS modeling efforts at the Naval Research Laboratory (NRL) using the NRL Layered Ocean Model (NLOM). Metzger and Hurlburt (1996) used a $1/2^\circ$ 1.5-layer reduced gravity global version of NLOM to study the coupled dynamics of the SCS and the Pacific Ocean. It focused on the upper ocean flow through Luzon Strait and the associated dynamics. As computing power increased, finer horizontal and vertical resolution was feasible in NLOM. Metzger and Hurlburt (2001b) examined the nondeterministic nature of Kuroshio intrusion and eddy shedding in the SCS on annual and interannual time scales using a $1/8^\circ$, 6-layer Pacific basin north of 20°S version of NLOM that included realistic bottom topography. At these time scales,

Kuroshio intrusion was found to be highly nondeterministic and not positively correlated to the interannual variations in the atmospheric or oceanic environment. However, the $1/8^\circ$ NLOM results indicated a model sensitivity to the resolution of the atmospheric forcing. Namely, the mean wind stress curl dipole over Luzon Strait in the 2.5° resolution ECMWF Operational 1000 hPa winds is double the strength of the 2.5° resolution ECMWF Reanalysis 1000 hPa winds for the same period, and this is greater than the interannual variability over this region. The difference is attributed to the spectral resolution of the two atmospheric models and the degree of spectral truncation performed by ECMWF before distribution on the 2.5° grid. Simulations forced with these ECMWF Operational winds exhibited deeper Kuroshio penetration, suggesting that the larger negative curl over the northern Luzon Strait created more Ekman pumping, a deepening of the thermocline, and increased intrusion. The Operational winds also produced a more detailed upper ocean circulation field throughout the SCS basin in $1/8^\circ$ NLOM (Metzger and Hurlburt, 2001b).

Progressing to even finer horizontal resolution, Metzger and Hurlburt (2001a) used a $1/16^\circ$ 6-layer Pacific version of NLOM to study the importance of resolution and coastline geometry in modeling SCS inflow via Luzon Strait. The increased horizontal resolution allowed a more accurate representation of the island chain and associated shoals in Luzon Strait which in turn had a significant impact on the mean pathway of the modeled Kuroshio. In $1/16^\circ$ NLOM, forced with a climatology based on the 1.125° resolution ECMWF Reanalysis 10 meter winds, the Kuroshio does not intrude into the SCS nearly as much as its $1/8^\circ$ resolution NLOM counterpart forced with 2.5° resolution ECMWF Reanalysis 1000 hPa winds. The study suggests that $1/16^\circ$ resolution is needed to adequately represent the islands and shoals in Luzon Strait and thus simulate a Kuroshio intrusion that is more consistent with observations. Otherwise, the modeled circulation in the northern SCS may be biased by the strongly inertial Kuroshio intruding too far into the SCS.

To help answer some of the questions raised in this introduction, the paper is laid out as follows. The numerical ocean model and wind forcing are described in Section 2. Section 3 provides details on the general description of the mean atmospheric and oceanic circulation. The ocean model response to atmospheric wind forcing is discussed in Section 4 and the paper ends with a summary and conclusions.

2. The Numerical Model and Wind Forcing

2.1 NLOM description

The semi-implicit, primitive equation ocean model used here is essentially the same as that described in

Table 1. Characteristics of wind forcing data sets.

Product	Resolution	NCAR data set ^(a)	Type	NLOM expt. name
HR	2.0°	DS232.0	surface stress	HR
ECMWF 10m	2.5 ^{α(b)}	DS115.0	10 m winds ^(c)	EC10m-2.5°
ECMWF 10m	1.125 ^{α(d)}	DS115.3	10 m winds ^(c)	EC10m-1.125°
ECMWF stress	1.125 ^{α(d)}	DS115.5	surface stress	ECstr
NCEP/NCAR	1.875 ^{α(e)}	DS090.0	surface stress	NCEP

^(a)The NCAR data set number is provided to clarify the products used in this study and allow the interested reader to learn more about each wind set at the NCAR website listed in the text.

^(b)The original ECMWF Reanalysis (ERA-15) used a model with a T106 spectral resolution/N80 Gaussian grid. In this data set ECMWF truncated these data to T47 (3.8° along the equator) and then interpolated to a 2.5° Cartesian grid. Note also that ECMWF is performing a second forty year reanalysis (ERA-40) with a T159 spectral model. This will be completed in early to mid 2003.

^(c)Wind velocities are converted to wind stress using the formulation of Kara *et al.* (2002). See the text.

^(d)These ERA-15 data are distributed on a N80 Gaussian grid. Longitudinal resolution is 1.125° but only approximately this resolution in latitude.

^(e)The NCEP Reanalysis model has T62 spectral resolution. Data are distributed on either a 2.5° Cartesian or Gaussian grid. On the Gaussian grid, the longitudinal resolution is 1.875° but only approximately this resolution in latitude.

Metzger and Hurlburt (2001b), except for the horizontal resolution and viscosity/diffusivity parameters. It is a 6-layer, thermodynamic, finite depth version of NLOM that includes realistic bottom topography. The horizontal resolution of each prognostic model variable is 1/16° (~7 km) in latitude by 45/512° (~9 km at 15°N, the mid-latitude of the SCS) in longitude. The model domain covers the Pacific Ocean from 20°S to 62°N and 109.125°E to 77.21°W, but the focus here is on the SCS. The fact that this is a basin-scale model eliminates the need to prescribe boundary conditions at the SCS inflow/outflow ports and allows direct connectivity between the deep ocean and this semi-enclosed sea via Luzon Strait.

The 1/12° ETOPO5 bottom topography (National Oceanic and Atmospheric Administration (NOAA), 1986) is used to define the model land-sea boundary, which is typically the 200 m isobath, but there are a few exceptions. Taiwan Strait and two interior Philippines passages, Leyte Gulf (125.5°E, 10.5°N) and San Bernadino Strait (124.5°E, 8.0°N), are opened at the 25 m isobath. Depth-weighted friction restricts the flow to realistic values in Taiwan Strait (see Metzger and Hurlburt, 2001b for details). The model boundaries are closed along 20°S, at the southern Indonesian archipelago, and at the Sunda Shelf in the southwest SCS. Metzger and Hurlburt (1996) and Metzger and Hurlburt (2001b) point to global versions of NLOM that found closing the Pacific to Indian Ocean throughflow and the Sunda Shelf did not significantly impact the simulated circulation in the SCS.

The primary model forcing is the surface momentum flux via the wind stress. The different wind data sets will be described in the next subsection and their forcing is the only difference in all the model experiments pre-

sented. Of secondary importance is the relaxation of the density fields to an annual mean climatology based on the Modular Ocean Data Assimilation System (Fox *et al.*, 2002). This relaxation can affect horizontal density gradients that in turn can generate density driven currents, but the effect is typically small compared to layer thickness gradients. No heat flux forcing is applied in the experiments used here because the focus of this paper is on upper ocean sensitivity to winds.

2.2 The wind forcing data sets

One observation-based wind set (HR) and climatologies based on numerical weather prediction models run at ECMWF and NCEP are used to force the ocean model. The HR monthly data set has enjoyed longstanding use in NLOM because of its early existence and because it produces realistic basin-wide circulation patterns across the Pacific Ocean. Wind data from ECMWF (Gibson *et al.*, 1999) and NCEP (Kalnay *et al.*, 1996) are chosen over Fleet Numerical Meteorology and Oceanography Center (we have data over the period June 1990–present) for several reasons. 1) The former two centers have both performed a reanalysis that uses a constant data assimilation scheme and atmospheric forecast model and thus are unaffected by operational model upgrades. 2) The ECMWF and NCEP reanalyses overlap each other and a common time period (1979–93) has been chosen to form a climatology. The common time period eliminates potential differences associated with the sampling period and the fifteen years are of sufficient length to produce a reasonable climatology. 3) The ECMWF and NCEP wind data have been more frequently used within the SCS modeling community. In forming the monthly

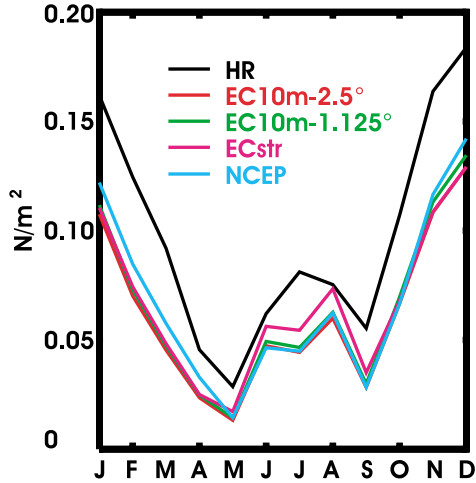


Fig. 2. Monthly wind stress magnitude averaged over the SCS basin for the five wind products: HR (black), EC10m-2.5° (red), EC10m-1.125° (green), ECstr (magenta) and NCEP (cyan). Units are N/m².

mean climatologies for ECMWF and NCEP, 6-hourly wind stress data are averaged.

Table 1 lists the characteristics of the individual wind products used in this study. All can commonly (but not exclusively) be obtained from the National Center for Atmospheric Research (NCAR) Data Support Section (<http://www.scd.ucar.edu/dss>). Note that several ECMWF products are investigated, all of which are derived from the original fifteen year ECMWF Reanalysis (ERA-15) (<http://www.ecmwf.int/research/era/ERA-15>). The difference between the first two ECMWF data sets is the horizontal resolution at which they are distributed. The latter two ECMWF data sets are different products but at the same horizontal resolution. The ECMWF 10 meter winds are analysis fields output by the atmospheric model and have been converted to wind stress after the formulae of Kara *et al.* (2002) that account for atmospheric stability.

$$\tau = \rho_a C_D (u^2 + v^2) \quad (1)$$

$$C_D = C_{D0} + C_{D1} (T_s - T_a) \quad (2)$$

$$C_{D0} = 10^{-3} [0.692 + 0.071 \widehat{V}_a - 0.00070 (\widehat{V}_a)^2] \quad (3)$$

$$C_{D1} = 10^{-3} [0.083 - 0.0054 \widehat{V}_a + 0.000093 (\widehat{V}_a)^2] \quad (4)$$

where τ is the wind stress, ρ_a is air density, C_D is the drag coefficient, u and v are the eastward and northward wind components, respectively, T_s is the sea surface tempera-

ture, T_a is the air temperature and V_a is the wind speed at 10 m. The ECMWF surface stresses are forecast fields output by the planetary boundary layer model within the larger atmospheric model. Hence these two products will be different even though they come from the same atmospheric model and have the same horizontal resolution. All forcing data sets have been interpolated to the model grid using cubic splines. Figure 2 shows the monthly SCS basin average wind stress magnitude for the five products. In general the curves from the numerical weather prediction models are very similar in amplitude, with the observational HR data stronger in all months. Harrison (1989) notes HR wind stresses tend to be strong because the drag coefficients used in the conversion of wind velocities to stresses were derived from the formula of Bunker (1976) rather than Large and Pond (1981).

3. General Description of the Mean Atmospheric and Oceanic Circulation

3.1 Mean atmospheric circulation

The annual mean wind stress curl is shown in Fig. 3. Recall that the numerical weather prediction products all span 1979–93 so as to eliminate differences associated with the sampling period. In general, the patterns are similar, suggesting the 15 year period chosen for the numerical weather prediction products is representative of the climatological (HR) conditions. Positive wind stress curl dominates the SCS basin with negative wind stress curl along the northern boundaries. However, there are some notable differences that exist in both the annual and monthly mean (shown later) wind analyses. The finer resolution EC10m-1.125° curl field (Fig. 3(d)) has more small scale structure and stronger maxima/minima than its coarser resolution counterpart, the EC10m-2.5° curl (Fig. 3(c)). This is consistent with the finding of Metzger and Hurlburt (2001b) who noted similar wind stress curl magnitudes differences associated with the varying spectral resolutions of the ECMWF Operational and Reanalysis models.

The most striking feature of the ECstr curl field (Fig. 3(e)) is the very small scale structure around the Philippines, Taiwan and Vietnamese coasts. This is not limited to the SCS basin but is a pervasive phenomenon along the land/sea boundary throughout the Pacific basin. The problem is most severe along coastlines with significant orographic features and are actually traces of Gibb's waves caused by the spectral truncation of the orography to 106 waves (P. Källberg-ECMWF Reanalysis Group, pers. comm.). The Gibb's waves are evident in all months. The ECMWF 10 m winds are post-processed differently than the ECMWF surface stress data and do not exhibit traces of the Gibb's waves.

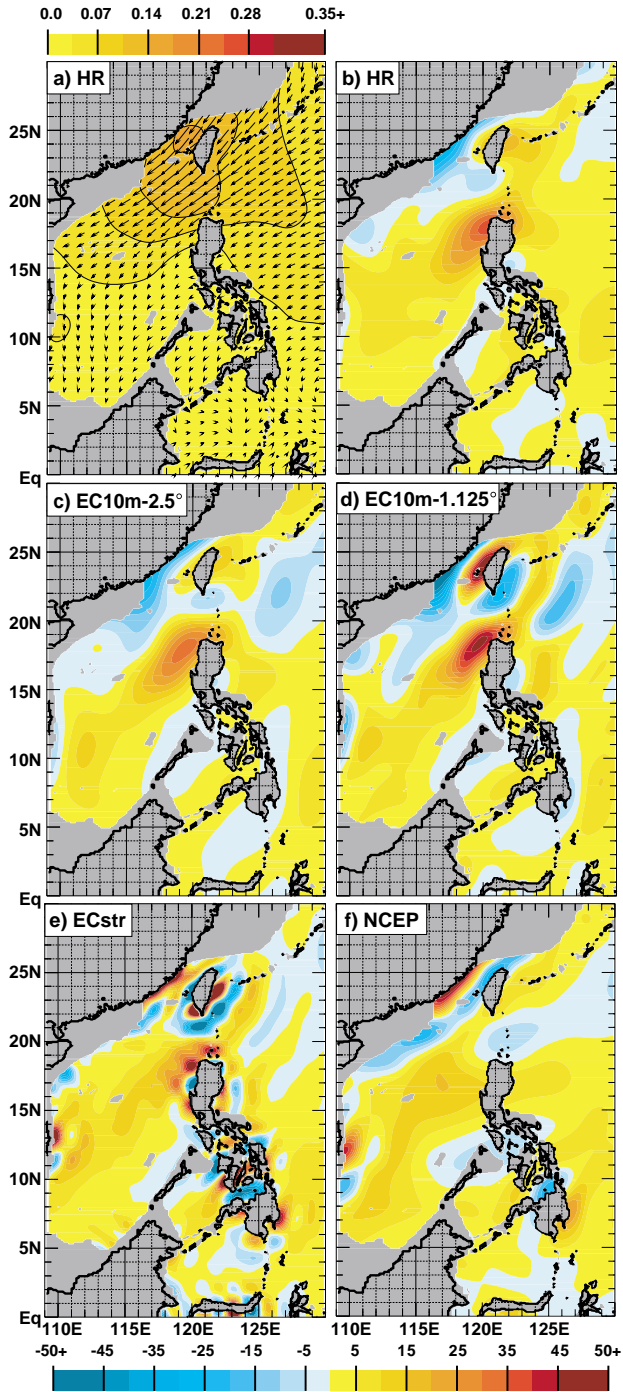


Fig. 3. Annual mean a) wind stress magnitude (Pa) and vectors for HR and wind stress curl ($\text{Pa}/\text{m} \times 10^{-8}$) for the five wind products used in this study: b) HR, c) EC10m-2.5°, d) EC10m-1.125°, e) ECstr and f) NCEP. Wind stress magnitude and vectors are shown for HR to provide a sense of the wind strength and direction, but are not included for all products due to space limitations. Positive wind stress curl is yellow/orange/red while negative wind stress curl is light blue/blue/dark blue. The contour interval for wind stress magnitude is .035 Pa (color bar at top) and $5 \text{ Pa}/\text{m} \times 10^{-8}$ for wind stress curl (color bar at bottom).

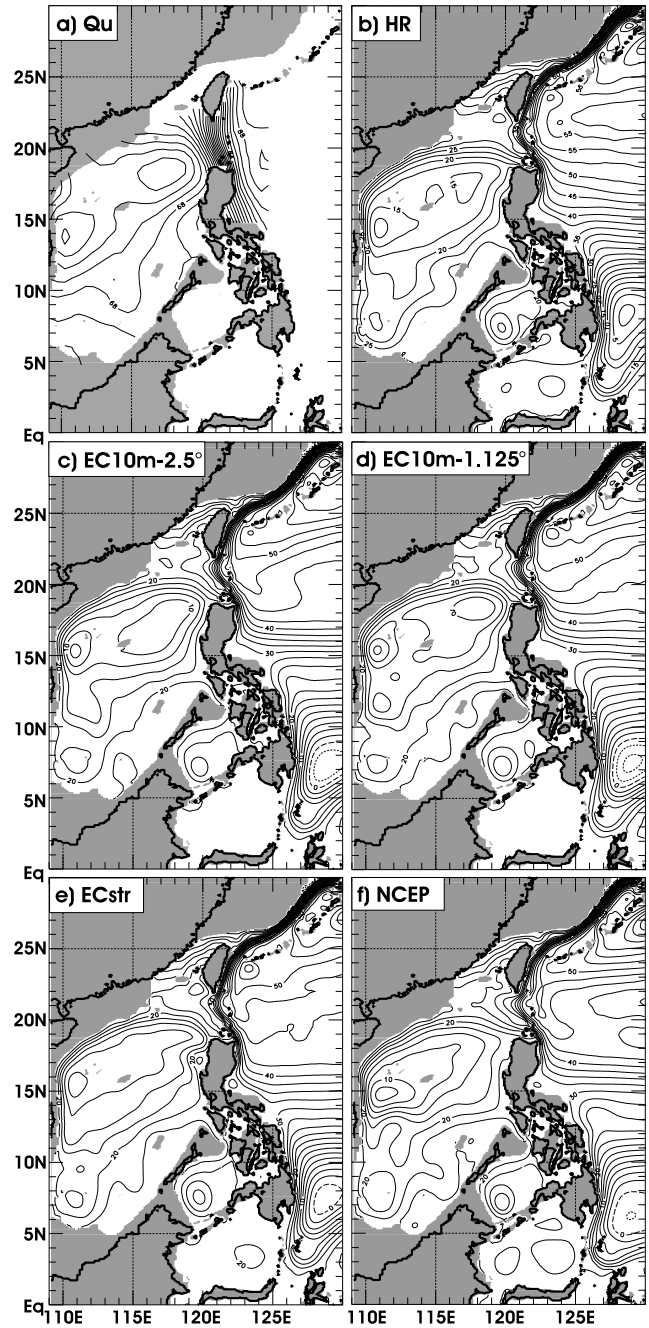


Fig. 4. Annual mean a) dynamic height at 100 m relative to 400 db adapted from Qu (2000) and sea surface height (SSH) from $1/16^\circ$ Pacific NLOM forced with b) HR, c) EC10m-2.5°, d) EC10m-1.125°, e) ECstr and f) NCEP wind products. The NLOM means span 6 years after the model has reached statistical equilibrium. The contour interval for dynamic height is 1 dyn cm and 2.5 cm for NLOM SSH.

Table 2(a). Mean volume transport^(a) across various sections from the 1/16°, 6-layer finite depth thermodynamic Pacific NLOM north of 20°S.

Transport section	Location		Experiment				
	Longitude, °E	Latitude, °N	HR	EC10m-2.5°	EC10m-1.125°	ECstr	NCEP
Luzon Strait ^(b)	121.1	18.5–22.5	-2.4	-2.2	-2.2	-2.0	-2.3
Taiwan Strait	118.4–120.6	24.5	1.1	0.9	0.9	1.1	0.9
East of Luzon	coast–124.6	18.0	12.3	10.9	9.2	11.3	13.0
East of Mindanao, 1	coast–134.4	8.0	-31.4	-28.7	-31.0	-29.3	-34.4
East of Mindanao, 2	coast–128.1	6.5	-36.8	-34.7	-32.6	-39.6	-36.1
Sibutu Passage	119.0–120.4	5.5	-2.4	-1.3	-1.4	-1.2	-1.4
San Bernadino Strait	124.1–124.3	12.6	-0.1	-0.1	-0.1	-0.2	-0.1
Leyte Gulf	125.2–125.5	10.0	0.0	0.0	0.0	-0.1	0.0

^(a)Transports are in Sverdrups ($1 \text{ Sv} \equiv 10^6 \text{ m}^3\text{s}^{-1}$) and for the sum of layers 1 through 6 except where noted. The mean covers a 6-year period after the experiment has reached statistical equilibrium. Positive transport is to the north (east) in east-west (north-south) oriented sections.

^(b)Transports are for the sum of layers 1 and 2 that have an average layer thickness of ~350 m.

Table 2(b). Standard deviation of volume transport across various sections from the 1/16°, 6-layer finite depth thermodynamic Pacific NLOM north of 20°S relative to the 6-year means in Table 2(a).

Transport section	Location		Experiment				
	Longitude, °E	Latitude, °N	HR	EC10m-2.5°	EC10m-1.125°	ECstr	NCEP
Luzon Strait	121.1	18.5–22.5	1.3	0.6	0.6	0.9	0.9
Taiwan Strait	118.4–120.6	24.5	0.2	0.2	0.2	0.1	0.1
East of Luzon	coast–124.6	18.0	16.1	12.3	15.3	12.8	12.3
East of Mindanao, 1	coast–134.4	8.0	12.5	10.9	10.9	11.8	10.0
East of Mindanao, 2	coast–128.1	6.5	20.9	20.1	18.6	23.4	14.5
Sibutu Passage	119.0–120.4	5.5	1.3	0.6	0.7	1.0	0.8
San Bernadino Strait	124.1–124.3	12.6	0.1	0.1	0.1	0.1	0.1
Leyte Gulf	125.2–125.5	10.0	0.2	0.1	0.2	0.1	0.1

The NCEP curl (Fig. 3(f)) is the most different of the wind products investigated. Of particular note is the lack of a strong positive wind stress curl maximum west of Luzon and a sign reversal of the curl dipole over Luzon Strait compared to the other products. Is the NCEP curl truly an outlier? Even though three ECMWF products are presented, they all come from the same atmospheric model. An examination (not shown) of the annual mean wind stress curl from the Southampton Oceanography Centre climatology and the Fleet Numerical Meteorology and Oceanography Center Navy Operational Global Atmospheric Prediction System (mean formed over 1990–1999) indicates they are much more consistent with the HR and ECMWF means than the NCEP mean. A second major difference found in the NCEP annual mean is the curl dipole off Vietnam. Apart from the ECstr mean adversely affected by Gibb's waves, this high-gradient wind stress curl dipole is not seen in any of the other wind sets.

3.2 Mean oceanic circulation

The seasonal upper ocean circulation in the SCS has been investigated through hydrographic observations, satellite altimeter data and numerical models. Hu *et al.* (2000) is a review article that collates many of these studies and offers a qualitative description of the seasonal currents. Based on hydrographic data, the basin-wide SCS circulation is cyclonic in winter and anti-cyclonic in summer. Winter-time cyclonic eddies exist off Luzon (West Luzon Eddy) and southeast of Vietnam. In summer a cyclonic eddy east of Vietnam (East Vietnam Eddy) and the Southeast Vietnam Offshore Current (Fang *et al.*, 1998) dominate the flow field in the central SCS while a broad anti-cyclonic eddy exists in the southern SCS.

Unfortunately, most hydrographic studies of the basin-wide circulation patterns are limited in areal extent and temporal coverage. Studies based on altimeter data fill these gaps and help complete our understanding of

the upper ocean flow. Shaw *et al.* (1999), Ho *et al.* (2000b), Hwang and Chen (2000) and Morimoto *et al.* (2000) corroborate the hydrographic data with regard to the basin-wide circulation and eddy field. However, altimeter based studies are confined to the time frame of the orbiting satellite and most published studies typically use five to six years of data. While this is long compared to hydrographic surveys, it is relatively short on climatological time scales. The satellite sampling period also covers a major El Niño event that is known to modify the SCS circulation (Chao *et al.*, 1996; Wu *et al.*, 1998; Ho *et al.*, 2000a; Hwang and Chen, 2000). Thus, altimeter-derived circulation patterns may not provide an accurate climatological picture of the upper ocean flow.

Qu (2000) saw a need for a more accurate description of the SCS circulation and used all available temperature profiles from the 1920's to early 1990's, along with climatological temperature and salinity relationships, and converted these to dynamic heights on a $0.5^\circ \times 0.5^\circ$ grid. These data of dynamic height at 100 m (relative to 400 db) provide the most complete climatological view of the upper ocean SCS circulation and will be the primary set of observations to which simulated results are compared.

The dynamic height data from Qu (2000) and the ocean model response are seen in Fig. 4. In general, NLOM reproduces the annual mean qualitatively well, but obvious differences exist. Some differences are associated with the varying wind products (which will be discussed in more detail in the next section), while other differences are associated with limitations in the model and observational data. The focus is first on the model and observational results along with a general description of the overall mean circulation.

One of the limiting factors within NLOM is the use of the 200 m isobath as the land/sea boundary. This has the effect of producing a tighter gradient in western boundary current in the northwest SCS compared to the dynamic heights. However, the observational analysis is on a $0.5^\circ \times 0.5^\circ$ grid that has insufficient resolution to adequately depict this boundary current. This lack of sufficient resolution is also evident within the Luzon Strait region. In addition, the comparison of the circulation in the southern SCS is more difficult because the dynamic height data suffer from a lack of observations south of a line from 109°E , 7°N to 120°E , 13°N and NLOM has a closed boundary at the Sunda Shelf. The effect of the closed boundary is a topic of further investigation at NRL, although previous studies indicate the impact is not significant.

Mean transports and variability are listed in Tables 2(a) and (b) respectively for various sections within the domain of interest. For those sections where observational transport data exists, the model experiments are gener-

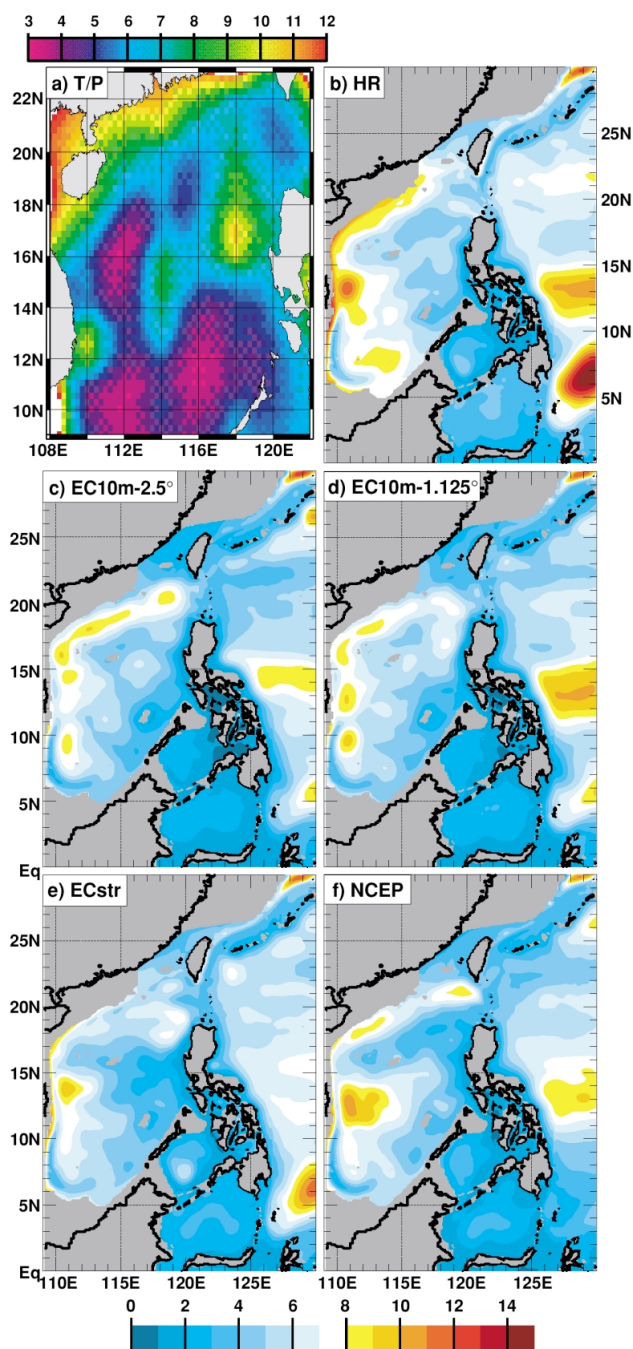


Fig. 5. Standard deviation of SSH from a) TOPEX/POSEIDON altimeter data relative to the 1993–1996 mean (adapted from Ho *et al.* (2000a)) and from $1/16^\circ$ Pacific NLOM forced with b) HR, c) EC10m-2.5°, d) EC10m-1.125°, e) ECstr and f) NCEP wind products relative to the six-year means in Fig. 4. The contour interval for the model-derived variability is 1 cm (color bar at bottom).

ally within the range of estimates. Of particular note, Qu (2000) and Liang *et al.* (2003) both estimate a net Pacific to SCS transport through Luzon Strait of 3 Sv within the upper 300–400 m. The NLOM values are reasonable, but lower than the observational estimates.

While the mean SSH in NLOM shows qualitative agreement with observed data, the SSH variability fields (Fig. 5) show more differences when compared to altimeter-derived variability fields. Possible reasons for the discrepancies include the use of monthly wind forcing in NLOM. Modeling experience has shown that lack of high frequency wind forcing has a substantial impact on the SSH variability in this region as simulations forced with monthly winds have reduced variability compared to those forced with interannual winds. In addition, the model is forced with monthly winds derived from a different period than the satellite observations.

Both Ho *et al.* (2000a) (Fig. 5(a)) and Hwang and Chen (2000) note three areas of high SSH variability (as do the dynamic height analyses of Qu (2000)). From highest to lowest these are the areas 1) west of Luzon (118°E, 17°N), 2) east of Vietnam (110°E, 13°N) and 3) the central SCS (114°E, 15°N). But all model simulations produce higher SSH variability in the region of the East Vietnam Eddy than west of Luzon. A corridor of high SSH variability is also seen along a southwest-northeast line in the northern SCS in NLOM that corresponds to a line of relatively low variability in the altimeter data. In NLOM, small scale eddies are sometimes generated southwest of Taiwan Strait. As these propagate to the southwest along the model boundary, they may amplify and contribute to the high variability corridor. They also terminate in the vicinity of the East Vietnam Eddy increasing the variability in this region.

4. Ocean Model Response to Atmospheric Wind Forcing

In comparing the NLOM simulated SSH with the observational dynamic height data, some differences are clearly a response to the wind forcing. Monthly mean wind stress curl is presented for February, May, August and November (Figs. 6, 8, 10 and 12, respectively) along with the corresponding monthly mean dynamic height and NLOM SSH (Figs. 7, 9, 11 and 13, respectively). What follows is a discussion of the pertinent findings.

4.1 Effect of winds on Kuroshio intrusion

As noted earlier, using 1/8° NLOM, Metzger and Hurlburt (2001b) found a sensitivity of the Kuroshio's intrusion into the SCS associated with the strength of the wind stress curl dipole over Luzon Strait. This appeared to be related to the spectral resolution and truncation method of the ECMWF 1000 hPa wind forcing. It was hypothesized that the stronger negative wind stress curl

in the northern Luzon Strait increased the Ekman pumping, deepening the model interfaces and leading to increased westward intrusion of the Kuroshio before retroflecting back to the east. However, using 1/16° NLOM forced with the same EC10m-1.125° winds used here (Fig. 3(d)) and having a strong wind stress curl dipole over Luzon Strait, Metzger and Hurlburt (2001a) indicated that the mean pathway of the Kuroshio within Luzon Strait is highly dependent upon the accuracy of the coastline geometry and how well the complex islands and shoals are resolved. But because two different atmospheric products are used (1000 hPa versus 10 meter winds) in these two studies, it cannot be unequivocally stated that coastline geometry is governing Kuroshio intrusion.

Further evidence is found in this study by noting a large difference in the magnitude of the negative wind stress curl over the northern Luzon Strait between the various wind products. The EC10m-1.125° and ECstr (Figs. 3, 6, 12 panels (d), (e)) have strong negative curl in the northern Luzon Strait while HR and EC10m-2.5° exhibit weaker negative curl (Figs. 3(b), (c) and 6(b), (c)). Moreover, NCEP has broad, albeit weak, negative wind stress curl over entire Luzon Strait (Figs. 3(f) and 12(f)). So the EC10m-1.125° and ECstr (HR and EC10m-2.5°) experiments have a wind environment similar to that which produced deeper (shallower) Kuroshio intrusion in 1/8° NLOM. Yet a comparison of Figs. 4, 7, 9, 11 and 13 reveals that Kuroshio intrusion is similar in all experiments in all months and thus the coastline geometry appears to be governing intrusion with little impact from the varying wind stress curl.

Because the dynamic height data cannot properly resolve the Kuroshio, I turn to a study by Liang *et al.* (2003) that composited approximately ten years of shipboard acoustic doppler current profiler data around Taiwan. Table 3 lists the v-velocity characteristics of the Kuroshio in Luzon Strait. The longitude of the northward v-velocity core in NLOM agrees extremely well with the observations, although the magnitude is low in all cases. The last column lists the longitude at which the v-velocity is reduced by one e-folding value. All simulations produce the same e-folding longitude except that forced by NCEP, and it is only slightly farther west even though Fig. 4(f) would seem to indicate somewhat broader, deeper Kuroshio intrusion. All experiments are slightly east of the e-folding longitude estimated from the observations.

One final note that indicates NLOM is producing a realistic intrusion of the Kuroshio into the SCS comes from Hwang and Chen (2000) who computed velocities at TOPEX/Poseidon crossover points. At a point west of Luzon Strait (~119°E, ~21°N) they note mostly northeastward or eastward flow in spring/summer and mostly southwestward or westward flow in winter. NLOM typically follows this pattern for most experiments.

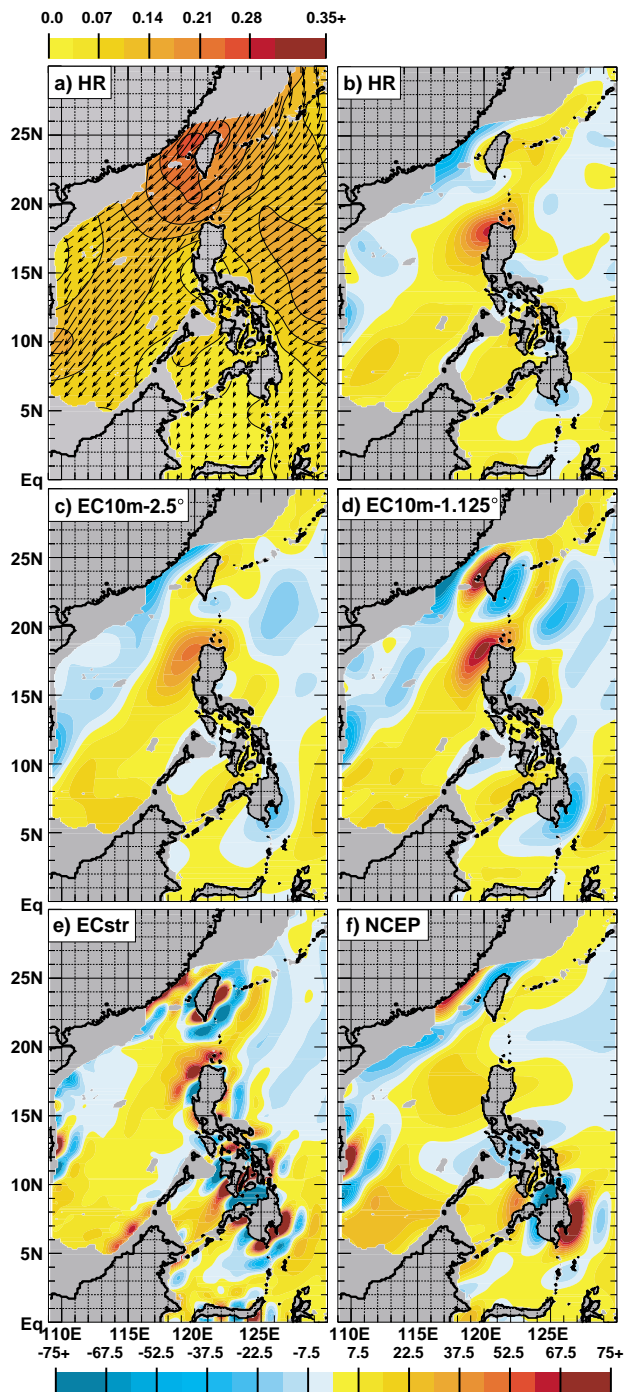


Fig. 6. As in Fig. 3 except for February. The contour interval for wind stress magnitude is .035 Pa (color bar at top) and $7.5 \text{ Pa/m} \times 10^{-8}$ for wind stress curl (color bar at bottom).

4.2 Generation of the West Luzon Eddy

The West Luzon Eddy is the dominant observed feature in the northern SCS (Figs. 4(a), 7(a), 9(a) and 13(a)). Shaw *et al.* (1999) performed an empirical orthogonal function (EOF) analysis on TOPEX/Poseidon altimeter

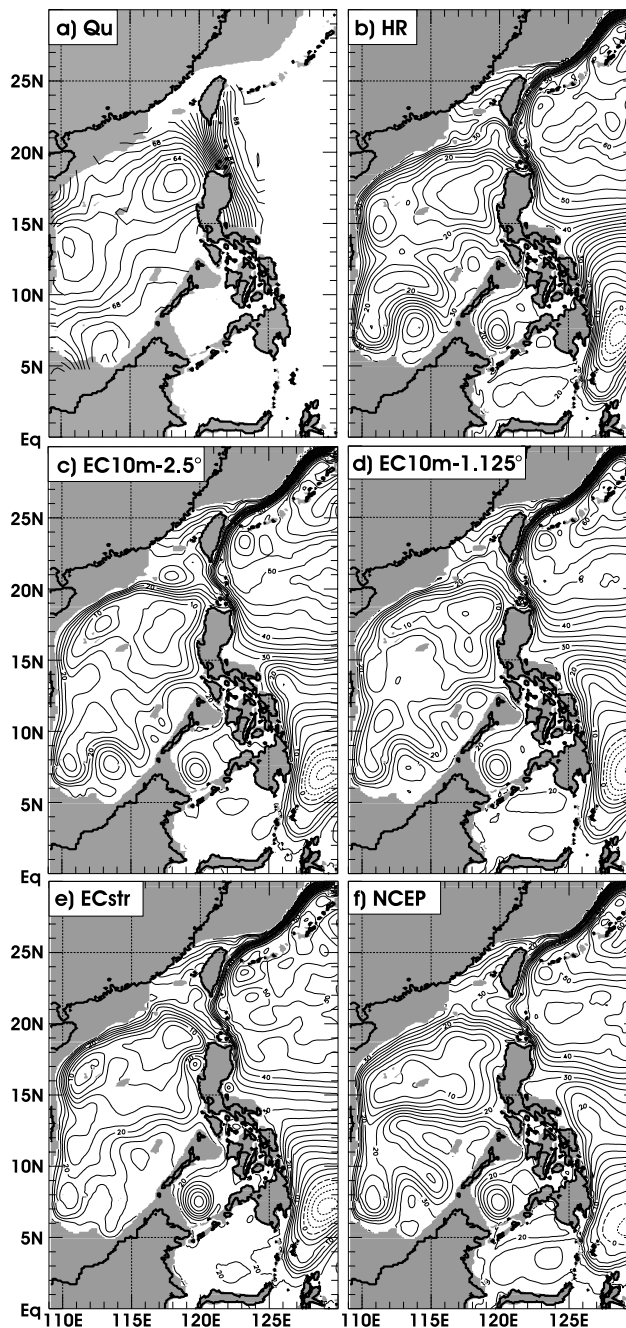


Fig. 7. As in Fig. 4 except for February. The dynamic height analysis is a three month mean centered on February.

data and wind stress curl from NCEP. They concluded that the sea level variations in the West Luzon Eddy could not be explained by wind stress curl. However, as noted above, positive wind stress curl west of Luzon is significantly different in NCEP compared to all other products. Perhaps this is why Shaw *et al.* (1999) could not find a causal relationship between sea level and wind stress curl variability in this region.

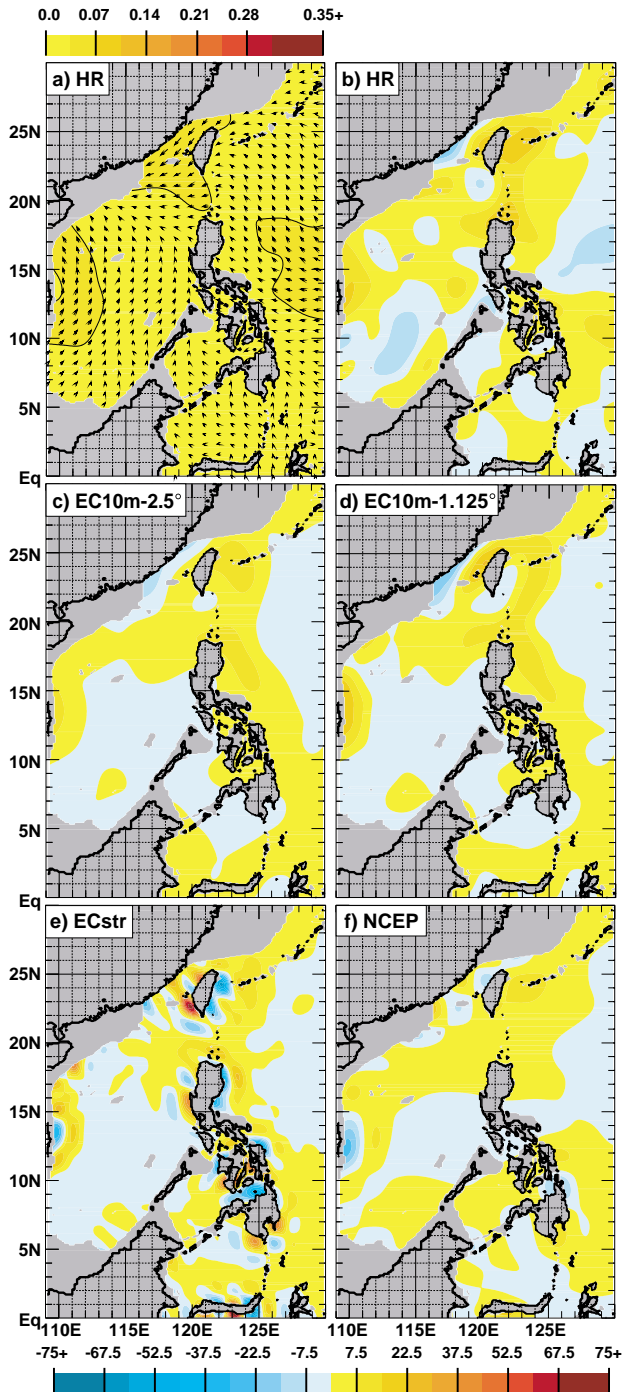


Fig. 8. As in Fig. 6 except for May.

Qu (2000) suggests that wind stress curl or direct Ekman pumping plays a major role in generating the West Luzon Eddy and the NLOM results support this hypothesis. Those experiments with a broad, distinct positive wind stress curl bullseye west of Luzon (panels (b)–(d) in Figs. 3, 6 and 12) produce a distinct West Luzon Eddy

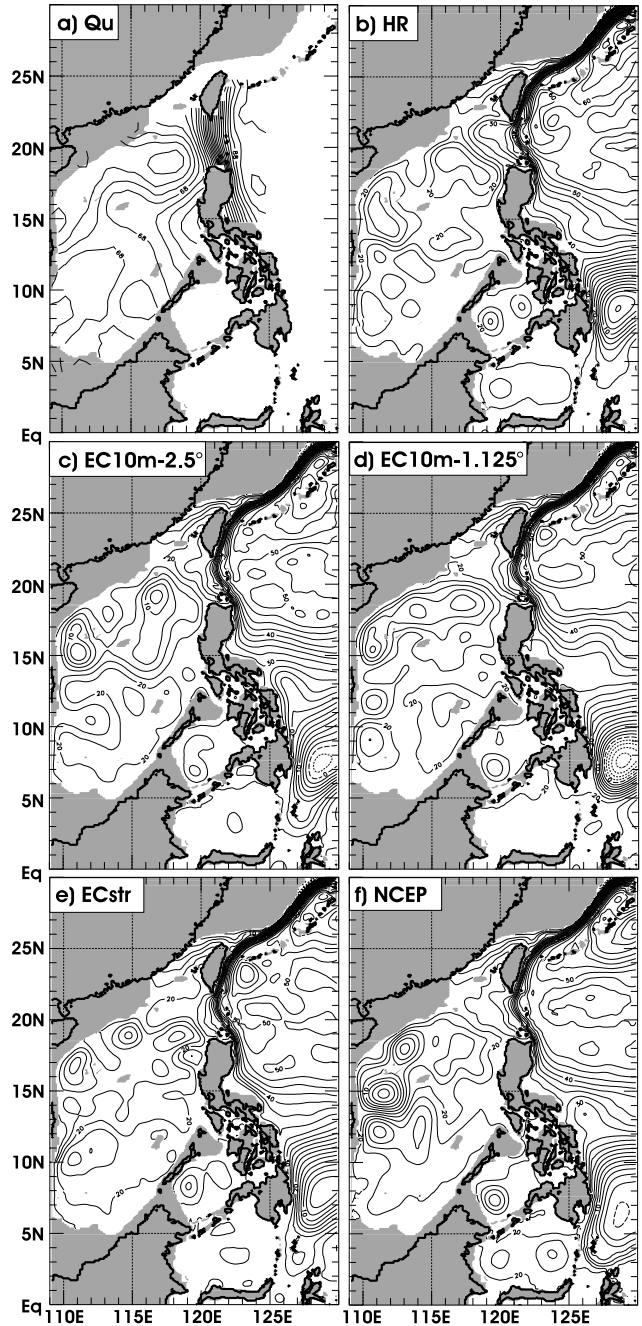


Fig. 9. As in Fig. 7 except for May.

in NLOM (panels (b)–(d) in Figs. 4, 7 and 13) that is consistent with the dynamic height data (Figs. 4(a), 7(a) and 13(a)). The EC10m-1.125° simulation produces a smaller, more distinct West Luzon Eddy in response to the tighter gradients and increased magnitude of the wind stress curl bullseye. The area of positive wind stress curl west of Luzon in ECstr (Figs. 3(e), 6(e) and 12(e)) is somewhat interrupted and broken up by the spurious nega-

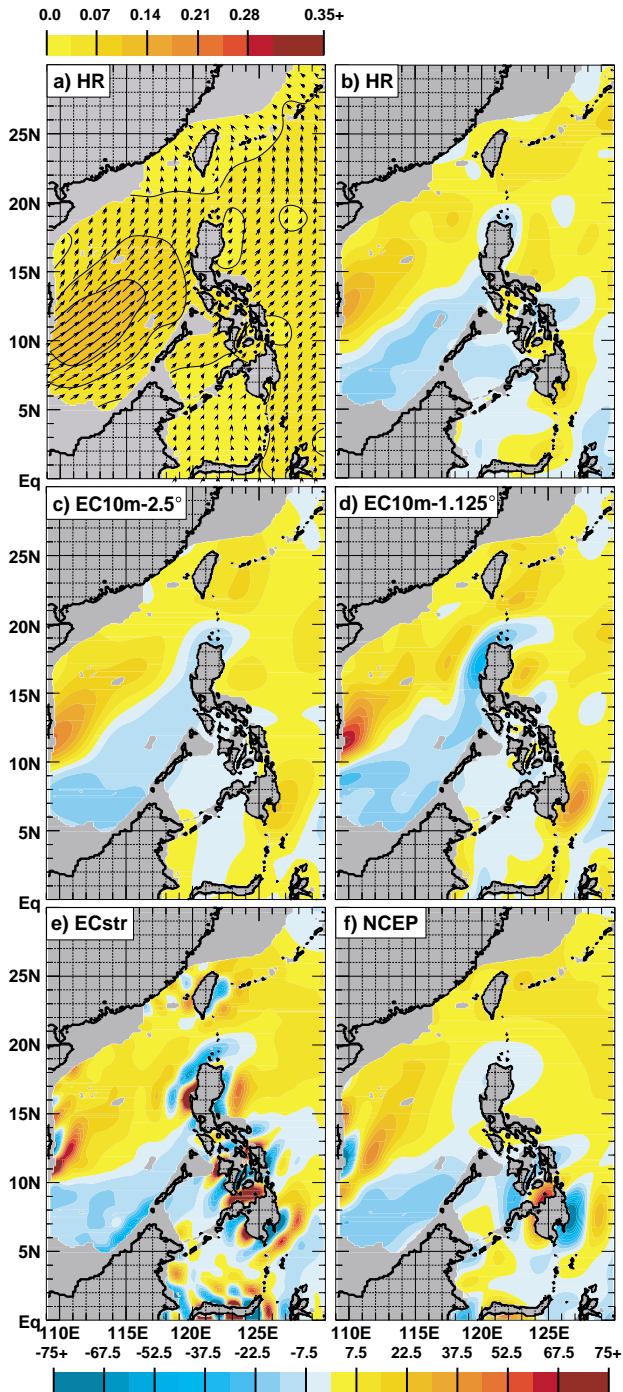


Fig. 10. As in Fig. 6 except for August.

tive coastal curl (120°E , 17°N) caused by Gibb's waves. In the annual mean (Fig. 4(e)), the simulated West Luzon Eddy is no longer a closed circulation but part of the basin-wide cyclonic flow. The NCEP forced simulation, which lacks a strong positive wind stress curl bullseye, does not produce a closed West Luzon Eddy but a broad

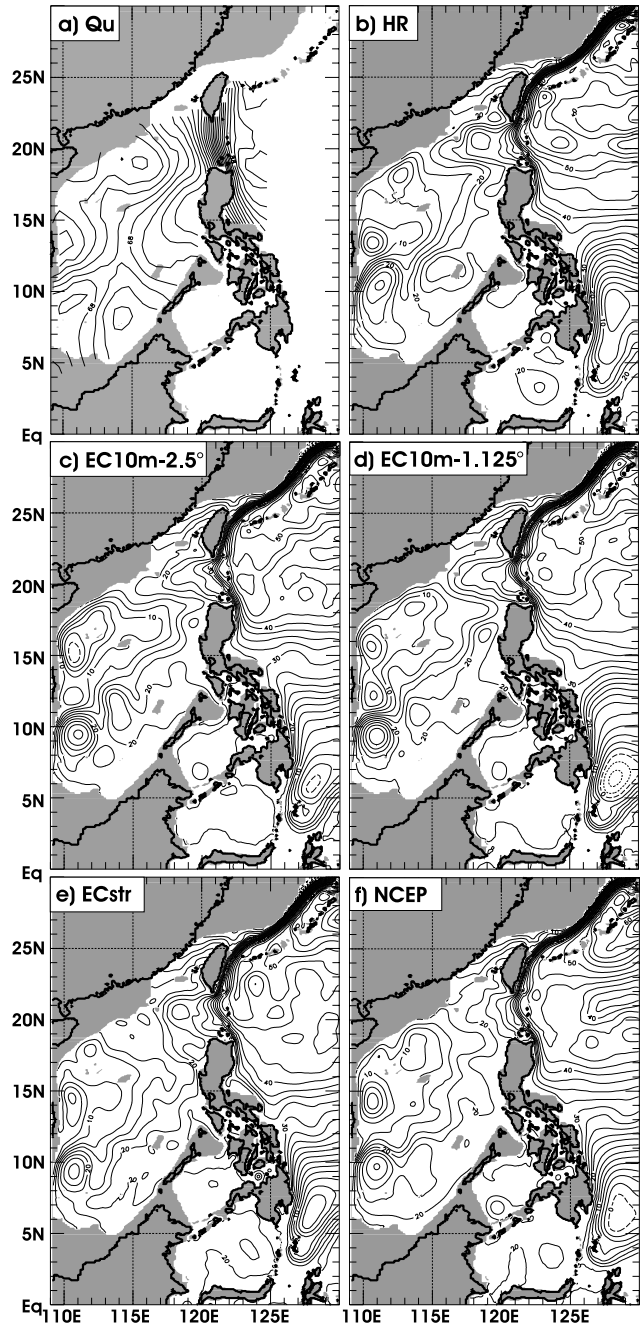


Fig. 11. As in Fig. 7 except for August.

central basin cyclonic circulation (Figs. 4(e), 7(e) and 13(e)).

To quantify the relationship between wind stress curl west of Luzon and the strength of the West Luzon Eddy, correlation coefficients (Table 4) are computed over the region $115^{\circ}\text{--}120^{\circ}\text{E}$, $17^{\circ}\text{--}20^{\circ}\text{N}$, i.e. the region that defines the West Luzon Eddy in the dynamic height data (Fig. 4(a)). By lagging the SSH data one month, maximum

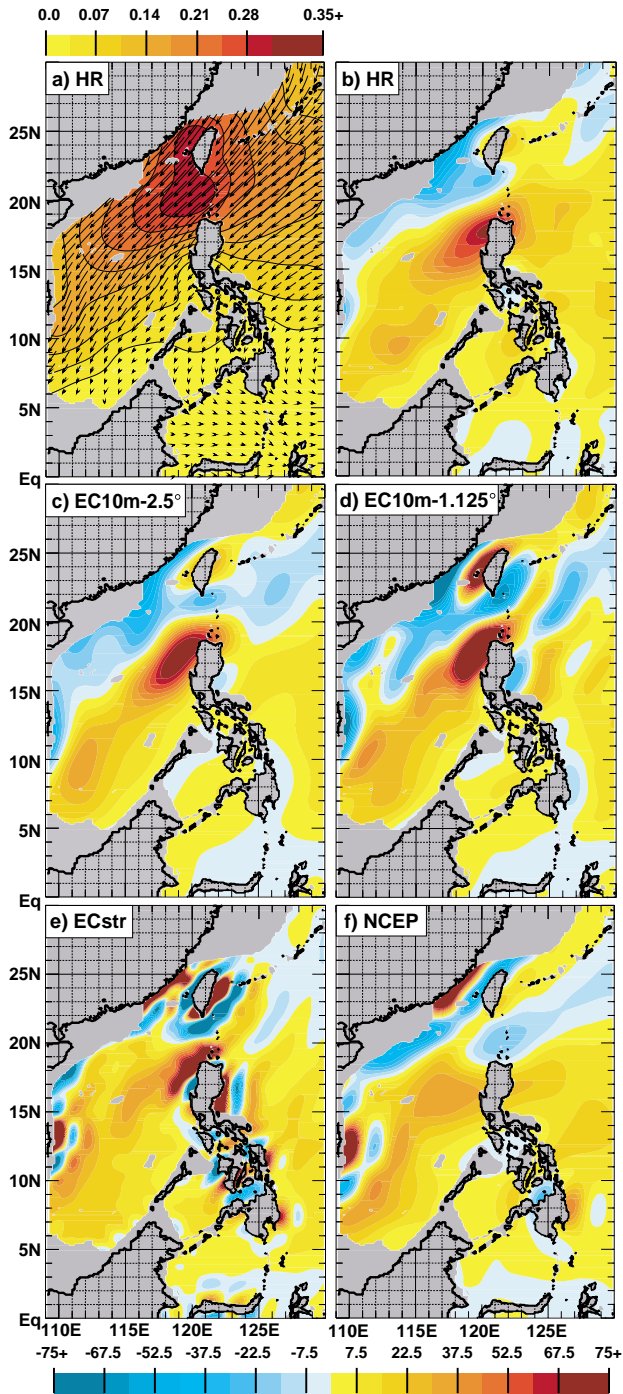


Fig. 12. As in Fig. 6 except for November.

correlation was obtained in all experiments except the one forced with NCEP stresses. Those experiments forced with ECMWF products produce the highest correlations, yet the correlation for the NCEP-forced simulation is still relatively high. However, a time series of the NCEP data (not shown) indicates the seasonal variability of both the

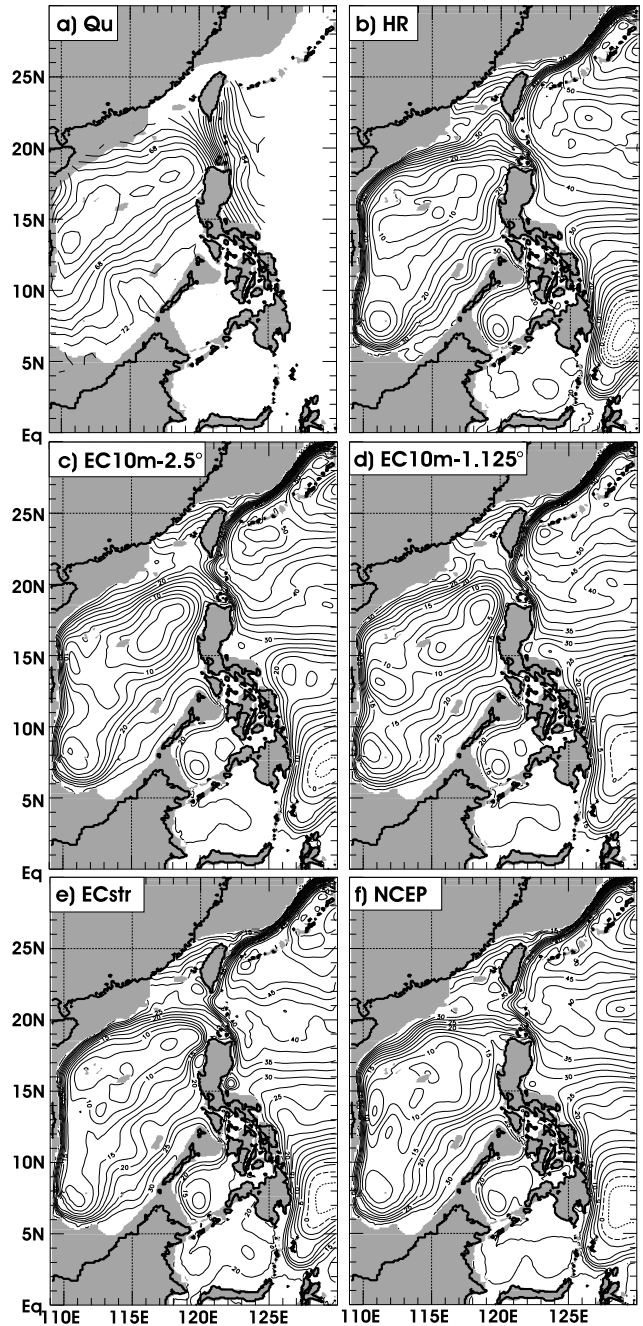


Fig. 13. As in Fig. 7 except for November.

wind stress curl and SSH over this subregion is much lower than the others. The seasonal cycle of the HR stresses and the accompanying ocean model SSH response is comparable to ECMWF, but it may produce lower correlations because the center of the wind stress curl bullseye straddles the land/sea coastline rather than being exclusively over the open ocean (Fig. 3(b)).

Table 3. Northward velocity characteristics of the Kuroshio within Luzon Strait^(a).

Source or experiment	Longitude of northward velocity core (°E)	Maximum northward velocity (cm s ⁻¹)	Longitude of e-fold northward velocity (°E)
Liang <i>et al.</i> (2003)	121.0	~60	120.0
HR	121.1	52	120.4
EC10m-2.5°	121.0	46	120.4
EC10m-1.125°	121.0	48	120.4
ECstr	121.0	48	120.4
NCEP	121.0	33	120.3

^(a)As determined on an east-west transect through Luzon Strait at 21°N.

Table 4. Correlation coefficient^(a) between wind stress curl west of Luzon and the strength of the West Luzon Eddy^(b).

Experiment	Correlation coefficient
HR	-.82
EC10m-2.5°	-.94
EC10m-1.125°	-.95
ECstr	-.98
NCEP	-.82

^(a)Correlation based on lagging the SSH one month.

^(b)Wind stress curl and simulated SSH averaged over the region 115°–120°E, 17°–20°N.

4.3 The Vietnamese offshore flow

The dynamic height data for May (Fig. 9(a)) and August (Fig. 11(a)) suggest offshore flow from the Vietnamese coast that propagates southward with the advent of the southwest monsoon. This is corroborated by multi-channel sea surface temperature (MCSST) images presented by Kuo *et al.* (2000) who note an upwelling region (i.e. cooler SST) moving southward along the coast and extending about 200 km offshore between May and August 1997. They found upwelling intensity to be correlated with the alongshore wind stress component and suggest Ekman transport plays an important role inducing upwelling. Hwang and Chen (2000) also note the importance of wind stress rather than wind stress curl in generating coastal upwelling in this region.

The ocean model response east of Vietnam is quite varied in May (Figs. 9(b)–(f)). In general, NLOM exhibits offshore flow between 13–14°N, but the magnitude is highly variable and more zonally oriented than the dynamic heights suggest (Fig. 9(a)). Given the strength of the simulated offshore flow in the NCEP-forced experiment (Fig. 9(f)), one might expect it to have stronger alongshore winds than the other products (not shown), yet in fact the southwesterly flow is relatively weak. It

appears the anti-cyclonic gyre (111°E, 12°N) may be generated by the coastal negative wind stress curl bullseye (Fig. 8(f)) not seen in most other products.

In August, all simulations produce offshore flow between 10–12°N (Figs. 11(b)–(f)) with a large anti-cyclonic eddy to the southeast of Vietnam similar to that noted by Fang *et al.* (1998). The anti-cyclonic rotation of this eddy is consistent with the negative wind stress curl in the southern part of the basin. The location of the cyclonic East Vietnam Eddy is somewhat variable in NLOM. The simulations forced with ECMWF 10 meter winds produce a double cyclonic gyre (Figs. 11(c) and (d)) not supported by the observations. Qu (2000) indicates the East Vietnam Eddy can be partly explained by the wind stress curl from late summer to early fall, but the patterns of positive curl (Figs. 10(c) and (d)) do not give any indication as to why a double gyre might form. The center of the East Vietnam Eddy (110.5°E, 14.5°N) is one degree too far north in the ECstr and NCEP forced simulations (Figs. 11(e) and (f)), possibly in response to the positive wind stress curl maxima also being farther north in these products. There is also a more distinct separation between the centers of the two counter-rotating gyres on either side of the oceanic offshore flow in the NCEP forced simulation compared to the other experiments. The negative wind stress curl bullseye at 110°E, 12°N (Fig. 10(f)) produces a small-scale (~75 km) anti-cyclonic gyre that appears to play a role in separating the gyres.

A final comment related to the Vietnamese offshore flow regards the unrealistic extent of the basin-wide, zonal flow along 13–14°N in the NCEP forced simulation in autumn (Fig. 13(f)) and especially in winter (Fig. 7(f)), features not seen in the dynamic height analyses. The winter-time zonal flow is of sufficient strength to influence the annual mean (Fig. 4(f)). The cause of this zonal flow appears to be a first-order linear Sverdrup balance response to the atmospheric forcing. Similar to the Atlantic study of Townsend *et al.* (2000), 1/16° linear global simulations forced with some of the same wind products used in this study indicate varying degrees of zonal

flow across the central SCS basin (not shown). The simulation forced with NCEP winds exhibits stronger zonal flow than all other products.

4.4 Effects of the spurious coastal curl in ECstr

The spurious wind stress curl in the ECstr data has already been shown to adversely affect the annual signature of the West Luzon Eddy. Because of its high horizontal resolution, NLOM is responding to the spurious curl at very small scales. Note in Figs. 3(e), 6(e) and 12(e) the negative wind stress curl bullseye at 120°E, 17°N just west of northern Luzon. It produces a very small scale (~100 km) anti-cyclonic eddy in NLOM (Figs. 4(e), 7(e) and 13(e)). This anti-cyclonic gyre shifts the location of the West Luzon Eddy (Fig. 7(e)) approximately 1° northward of the location of the observed eddy. The ECstr positive wind stress curl bullseye at 122°E, 15.5°N, just east of Luzon, produces a relatively strong cyclonic eddy in NLOM. The other wind products also produce a small scale eddy east of Luzon (Figs. 4(f), 13(c), 13(d), 13(f)) but of smaller amplitude than the ECstr-forced simulation. In all cases the eddy has a circulation consistent with the wind stress curl, i.e. cyclonic circulation for positive wind stress curl and anti-cyclonic circulation for negative wind stress curl with the strength of the eddy proportional to the strength of the wind stress curl. It is hypothesized that these eddies result from an interaction between the bifurcation of the North Equatorial Current and the coastline geometry. The high-speed core of the North Equatorial Current does not penetrate all the way to the coast but turns northward, leaving an area of relatively slow currents near 122°E, 15.5°N that is influenced by the wind stress curl. Nonetheless, as seen by the example west of Luzon, the implications of this spurious curl would extend to all high horizontal resolution models since this problem is pervasive throughout this data set, especially near coastlines with significant orographic features.

5. Summary and Conclusions

A 1/16° Pacific Ocean version of the NRL Layered Ocean Model has been used to investigate the sensitivity of the upper ocean circulation in the SCS to various atmospheric wind forcing products. Five different monthly mean climatologies were used to force NLOM. They include the observation-based Hurrell and Rosenstein (1983) wind stresses (2.0° Cartesian grid), three products from the initial ECMWF Reanalysis (10 meter winds on a 2.5° Cartesian grid, 10 meter winds and surface wind stresses both on a 1.125° Gaussian grid) and surface stresses from the NCEP Reanalysis (1.875° on a Gaussian grid). The climatologies from the numerical weather prediction models are formed over the same time period (1979–93) to avoid differences associated with the sampling period. Significant differences exist in the wind

stress curl patterns and this is reflected in the upper ocean model response that is compared to observational data and analyses.

Using 1/8° NLOM, Metzger and Hurlburt (2001b) found a sensitivity of Kuroshio intrusion into the SCS via Luzon Strait to the spectral resolution of the ECMWF winds. In that study, it was noted how the ECMWF Operational model produced a wind stress curl dipole over Luzon Strait with larger extrema than the ECMWF Reanalysis model. The difference in curl was attributed to the spectral resolution and truncation of the wavenumbers. The stronger negative wind stress curl in the northern Luzon Strait was thought to increase Ekman pumping, deepen the thermocline and increase the westward intrusion of the Kuroshio.

In the present study, a similar contrast exists in the strength of the wind stress curl dipole over Luzon Strait between the ECMWF 10 meter winds at 2.5° and 1.125° resolution (Figs. 3(c) and (d), respectively). In addition, the NCEP stresses exhibit broad negative wind stress curl over the entire Luzon Strait. Is Kuroshio intrusion equally as sensitive to the wind stress curl field over Luzon Strait at 1/16° resolution, or is it controlled by the accuracy of the coastline geometry of the island chain within the strait as pointed out by Metzger and Hurlburt (2001a)? The model experiments clearly indicate it is the latter. The degree of Kuroshio intrusion in 1/16° NLOM is not sensitive to wind forcing. The longitude of the maximum northward velocity core is identical in nearly all simulations and agrees with an observational cross-section (Table 3). In addition, the longitude at which the northward velocity decreases by one e-folding value is also insensitive to wind forcing.

The West Luzon Eddy is the dominant feature observed in the northern SCS. Using TOPEX/Poseidon altimeter data and NCEP wind stress curl, Shaw *et al.* (1999) performed an EOF analysis and concluded the variations in sea level associated with the West Luzon Eddy could not be explained by wind stress curl. However, the NCEP wind stress curl field lacks a strong positive bullseye west of Luzon while all other wind products exhibit such a feature. The model results here support the hypothesis of Qu (2000) who suggests wind stress curl plays a major role in generating the West Luzon Eddy. Those experiments with a broad, distinct positive wind stress curl bullseye west of Luzon (panels (b)–(d) in Figs. 3, 6 and 12) produce a distinct West Luzon Eddy in NLOM (panels (b)–(d) in Figs. 4, 7 and 13) that is consistent with the dynamic height analyses (Figs. 4(a), 7(a) and 13(a)). The NCEP forced simulation does not produce a closed circulation west of Luzon (Figs. 4(f), 7(f) and 13(f)).

Along the Vietnamese coast, an offshore oceanic jet forms in May between 13–14°N and propagates southward to 11–12°N by August. Based on MCSST images,

Kuo *et al.* (2000) suggest Ekman transport plays an important role inducing upwelling in the region. In addition they suggest that the deformation and movement of the upwelled cold water is associated with two mesoscale anti-cyclonic gyres seen in contemporaneous TOPEX/Poseidon altimeter data. Comparable $1/16^\circ$ NLOM simulations that include a mixed layer suggest the SST cooling is associated with the offshore flow between the counter-rotating dipole east of Vietnam (not shown). As the flow moves offshore, divergence at the coast requires cooler water to be upwelled.

On the north side of the offshore oceanic jet is the cyclonic East Vietnam Eddy while on the south side there is an anti-cyclonic gyre. In general, the simulations qualitatively reproduce the offshore oceanic jet and its southward propagation, but the corresponding eddy structure produced by the different wind sets varies substantially. No single experiment reproduces the locations of the counter-rotating gyres as depicted by the dynamic height observations. Experiments forced with similar wind stress curl patterns in this region respond differently. Thus it is hard to draw a causal relationship between it and the eddies.

The ECMWF surface stress product suffers from spurious wind stress curl along the coastal boundaries, especially in regions with significant orographic features (Figs. 3(e), 6(e), 8(e), 10(e) and 12(e)). This problem exists throughout this data set and is not limited to the SCS basin. The alternating bands of positive and negative wind stress curl are actually traces of Gibb's waves caused by the spectral truncation of the orography to 106 waves (P. Källberg-ECMWF Reanalysis Group, pers. comm.). This anomalous curl has serious implications to both the large and small scale. The large area of positive wind stress curl west of Luzon is broken up by the Gibb's waves and in the annual mean (Fig. 4(e)), the simulated West Luzon Eddy is no longer a closed circulation but part of the basin-wide cyclonic flow. On the smaller scale, because of its high horizontal resolution, NLOM responds to the spurious curl by producing very small scale (~ 100 km) coastal gyres. Use of this product in high resolution basin-scale or coastal models requires caution as erroneous coastal circulations may result.

The results listed above clearly indicate a high horizontal resolution model is regionally sensitive to the choice of atmospheric forcing, even when sampled over the same time period. While a quantitative claim cannot be made that one wind forcing set most accurately represents the climatological upper ocean circulation, deficiencies are pointed out in the various atmospheric products that lead to a spurious underlying oceanic response and thus the need for care in choosing atmospheric forcing products for high resolution ocean models and for care in interpreting the results.

Acknowledgements

This work was performed as part of the 6.1 Dynamics of the Low Latitude Western Boundary Currents project under program element 601153N sponsored by the Office of Naval Research. Gracious thanks are extended to Dr. Tangdong Qu for providing the dynamic height data, Dr. Chung-Ru Ho for the satellite-derived SSH RMS figure and Dr. Harley Hurlburt for useful discussions and advice. The numerical simulations were performed using grants of computer time from the Department of Defense High Performance Computing Modernization Office on Cray T3E computers at the Naval Oceanographic Office, Stennis Space Center, Mississippi and the Engineering Research and Development Center, Vicksburg, Mississippi. This work is NRL contribution number NRL/JA/7320-02-8 and has been approved for public release.

References

- Bunker, A. F. (1976): Computations of surface energy flux and annual air-sea interactions cycles of the North Atlantic Ocean. *Mon. Wea. Rev.*, **104**, 1122–1140.
- Chao, S. Y., P. T. Shaw and S. Wu (1996): El Niño modulation of the South China Sea circulation. *Prog. Oceanogr.*, **38**, 51–93.
- da Silva, A. M., C. C. Young and S. Levitus (1994): Algorithms and procedures. Vol. 1, Atlas of surface marine data. *NOAA Atlas NESDIS 6*, 74 pp.
- Fang, G. H., W. D. Fang, Y. Fang and K. Wang (1998): A survey of studies on the South China Sea upper ocean circulation. *Acta Oceanogr. Taiwanica*, **37**(1), 1–16.
- Fox, D. N., W. J. Teague, C. N. Barron, M. R. Carnes and C. M. Lee (2002): The Modular Ocean Data Assimilation System (MODAS). *J. Atmos. Oceanic Technol.*, **19**, 240–252.
- Gibson, J. K., P. Källberg, S. Uppala, A. Hernandez, A. Nomura and E. Serrano (1999): *ECMWF Re-analysis Project Report Series: 1. ERA-15 Description (Version 2 - January 1999)*. ECMWF, Reading, Berkshire, U.K., 74 pp.
- Harrison, D. E. (1989): On climatological monthly mean wind stress and wind stress curl fields over the World Ocean. *J. Climate*, **2**, 57–70.
- Hellerman, S. and M. Rosenstein (1983): Normal monthly wind stress over the World Ocean with error estimates. *J. Phys. Oceanogr.*, **13**, 1093–1104.
- Ho, C. R., N. J. Kuo, Q. Zheng and Y. S. Soong (2000a): Dynamically active areas in the South China Sea detected from TOPEX/Poseidon satellite altimeter data. *Remote Sens. Environ.*, **71**, 320–328.
- Ho, C. R., Q. Zheng, Y. S. Soong, N. J. Kuo and J. H. Hu (2000b): Seasonal variability of sea surface height in the South China Sea observed with TOPEX/Poseidon altimeter data. *J. Geophys. Res.*, **105**, 13981–13990.
- Hogan, P. J. and H. E. Hurlburt (2003): Sensitivity of simulated circulation to surface wind forcing in the Japan/East Sea. *Deep-Sea Res. Part II* (accepted).
- Hu, J., H. Kawamura, H. Hong and Y. Qi (2000): A review on the currents in the South China Sea: Seasonal circulation,

- South China Sea Warm Current and Kuroshio Intrusion. *J. Oceanogr.*, **56**, 607–624.
- Hwang, C. and S. A. Chen (2000): Circulations and eddies over the South China Sea derived from TOPEX/Poseidon altimetry. *J. Geophys. Res.*, **105**, 23943–23965.
- Josey, S. A., E. C. Kent and P. K. Taylor (1998): The Southampton Oceanography Centre (SOC) ocean-atmosphere heat, momentum, and freshwater flux atlas. *Southampton Oceanography Centre Report No. 6*, 30 pp. plus figs.
- Kalnay, E., M. Kanamitsu, R. Kistler, W. Collins, D. Deaven, L. Gandin, M. Iredell, S. Saha, G. White, J. Woollen, Y. Zhu, M. Chelliah, W. Ebisuzaki, W. Higgins, J. Janowiak, K. C. Mo, C. Ropelewski, J. Wang, A. Leetmaa, R. Reynolds, R. Jenne and D. Joseph (1996): The NCEP/NCAR 40-Year Reanalysis Project. *Bull. Amer. Meteor. Soc.*, **77**, 437–471.
- Kara, A. B., P. A. Rochford and H. E. Hurlburt (2002): Air-sea flux estimates and the 1997–1998 ENSO event. *Boundary-Layer Meteorology*, **103**, 439–458.
- Kuo, N. J., Q. Zheng and C. R. Ho (2000): Satellite observation of upwelling along the western coast of the South China Sea. *Remote Sens. Environ.*, **74**, 463–470.
- Large, W. G. and S. Pond (1981): Open ocean momentum flux measurements in moderate to strong winds. *J. Phys. Oceanogr.*, **11**, 324–336.
- Liang, W. D., T. Y. Tang, Y. J. Yang, M. T. Ko and W. S. Chuang (2003): Upper ocean currents around Taiwan. *Deep-Sea Res. Part II*, Special Issue on Kuroshio Edge Exchange Process (KEEP), **50**, 1085–1105.
- Liu, Z., H. Yang and Q. Liu (2001): Regional dynamics of seasonal variability in the South China Sea. *J. Phys. Oceanogr.*, **31**, 272–284.
- Metzger, E. J. and H. E. Hurlburt (1996): Coupled dynamics of the South China Sea, the Sulu Sea and the Pacific Ocean. *J. Geophys. Res.*, **101**, 12331–12352.
- Metzger, E. J. and H. E. Hurlburt (2001a): The importance of high horizontal resolution and accurate coastline geometry in modeling South China Sea inflow. *Geophys. Res. Lett.*, **28**, 1059–1062.
- Metzger, E. J. and H. E. Hurlburt (2001b): The nondeterministic nature of Kuroshio penetration and eddy shedding in the South China Sea. *J. Phys. Oceanogr.*, **31**, 1712–1732.
- Morimoto, A., K. Yoshimoto and T. Yanagi (2000): Characteristics of sea surface circulation and eddy field in the South China Sea revealed by satellite altimetric data. *J. Oceanogr.*, **56**, 331–344.
- National Oceanic and Atmospheric Administration (1986): ETOPO5 digital relief of the surface of the Earth. *Data Announcement. 86-MGG-07*, Natl. Geophys. Data Cent., Boulder, Colo.
- Qu, T. (2000): Upper-layer circulation in the South China Sea. *J. Phys. Oceanogr.*, **30**, 1450–1460.
- Shaw, P. T., S. Y. Chao and L. L. Fu (1999): Sea surface height variations in the South China Sea from satellite altimetry. *Oceanologica Acta*, **22**(1), 1–17.
- Townsend, T. L., H. E. Hurlburt and P. J. Hogan (2000): Modeled Sverdrup flow in the North Atlantic from 11 different wind stress climatologies. *Dyn. Atmos. Oceans*, **32**, 373–417.
- Wu, C. R., P. T. Shaw and S. Y. Chao (1998): Seasonal and interannual variations in the velocity field of the South China Sea. *J. Oceanogr.*, **54**, 361–372.